Decimeter Level Cooperative Direct Localization With Ising Model Approach

Shiva Akbari, *Graduate Student Member, IEEE*, and Shahrokh Valaee, *Fellow, IEEE*

***Abstract*— With the ubiquitous availability of WiFi signals, WiFi-based localization methods have gained a lot of attention, especially in indoor environments. Generally, accurate indoor localization is challenging due to the multipath effect. Numerous methods have been proposed to increase the accuracy of localization for multipath environments. One of the recent methods is *direct localization*. This method includes a two-dimensional search in a planar geometry to directly localize the source without estimating any intermediate variable such as angle-of-arrival or time-of-flight. In this paper, we use a compressed sensing framework in the direct localization technique to estimate the location of a user in an indoor multipath environment. We form a penalized ℓ_0-norm structure for this problem and then convert this structure to an Ising energy problem to take advantage of the efficient existing binary programming solvers. In this paper, the Ising energy problem is solved using Markov Chain Monte Carlo (MCMC). The evaluations show that our approach significantly improves the localization accuracy compared to other approaches in the literature.**

***Index Terms*— Direct localization, compressed sensing, sparse modeling, Ising model, Digital Annealer.**

I. Introduction

LOCATION-BASED services (LBS) are a category of applications and services designed to provide users with information or assistance related to their specific geographical position. In recent years, these services have gained considerable attraction, especially in applications such as navigation, tracking, augmented reality, etc. Accurate location information is crucial for these applications. Consequently, the field of localization has gained significant attention from both academia and industry. While the Global Positioning System (GPS) has proven highly effective for outdoor localization, it encounters challenges in indoor and harsh multipath environments. In these environments, GPS signals can be obstructed or distorted by structures, walls, and other physical obstacles. This can lead to imprecise location data, which is unsuitable for many LBS applications.

Manuscript received 16 October 2023; revised 27 March 2024; accepted 29 May 2024. Date of publication 19 June 2024; date of current version 11 October 2024. This work was supported in part by Fujitsu Ltd.; in part by Fujitsu Consulting (Canada) Inc.; and in part by the University of Toronto to access Digital Annealer. The associate editor coordinating the review of this article and approving it for publication was P. Casari. *(Corresponding author: Shiva Akbari.)*

The authors are with the Department of Electrical and Computer Engineering, University of Toronto, Toronto, ON M5S 2E4, Canada (e-mail: shiva.akbari@mail.utoronto.ca).

Color versions of one or more figures in this article are available at https://doi.org/10.1109/TWC.2024.3413671.

Digital Object Identifier 10.1109/TWC.2024.3413671

Addressing these challenges is important and researchers have proposed several algorithms to increase the precision of location estimation, especially within indoor environments. Moreover, the emergence of 5G and 6G networks, renowned for their enhanced positioning capabilities, holds considerable potential for more accurate location-based services. Recently, for indoor environments, WiFi-based localization methods have been developed [1], [2]. These methods rely on *channel state information* (CSI). CSI captures the amplitude and phase information of the transmitted signal and is utilized to estimate different signal parameters, such as the angle of arrival (AoA) and time of flight (ToF). These parameters can lead to different localization techniques [2]. One of the categories of WiFi-based localization uses the angle of arriving wavefront, AoA, to localize users [3], [4], [5], [6], [7], [8], [9]. In AoA-based methods, first, the AoA of the wavefront is retrieved from the outputs of the receiving antenna arrays. Next, the location of the user is estimated by triangulation.

There has been extensive research on increasing the accuracy and computational efficiency of AoA estimation techniques. One of the initial methods introduced for AoA estimation is beamforming, which extends the principles of Fourier-based spectral analysis [10]. Another class of techniques, known as the subspace-based algorithms, utilizes the second-order statistics of signals to estimate AoA. MUSIC [11] and ESPIRIT [12] are among these methods. While these algorithms are computationally efficient, they suffer from low accuracy, especially in scenarios with highly correlated signals [13]. To enhance the accuracy of AoA estimates, maximum-likelihood estimation techniques have been proposed. However, these methods require prior knowledge of the number of sources [14]. In recent decades, with the introduction of sparse representation and compressed sensing, AoA estimation techniques based on sparse modeling have been proposed [7], [8], [9], [15]. These methods recover a sparse signal in a domain from under-sampled linear measurements [16].

The existing AoA-based localization methods have acceptable performance in open-air environments where there is few reflections in the environment. However, these methods require a two-step procedure (AoA estimation and triangulation) that makes the solutions suboptimal [17], [18]. Recently, a direct positioning approach has been introduced [19], where the user's location is directly estimated from the received signal in the antenna arrays; it requires a search over the potential locations of the source [20]. In this method, no intermediate parameter, such as AoA or ToF, is

estimated. Thus, this approach is able to tackle the suboptimality problem.

The idea of direct localization was first developed in [20]. In that work, the authors proposed a one-step direct localization approach based on estimating the eigenstructure of the spectral density matrix of the received signal. After a few decades, in [19], the authors proposed a direct position determination (DPD) technique. They defined a closed-form cost function for matched-field processing using a two-dimensional search over the known locations of the emitter. Then, in [21], the DPD was extended to multiple sources. However, the DPD technique assumed a multipath-free environment. Later, in [22], the authors proposed a maximum likelihood estimation based on direct localization for a multipath environment with a known number of multipaths. In [22], authors proposed a direct location estimation (DLE) algorithm for a dense multipath environment based on a Gaussian approximation. This method requires the estimator to have prior knowledge of the power delay profile. Recently, Garcia et al. [23] presented a direct source localization (DiSouL) that jointly processes the received data in all the antenna arrays in a compressed sensing framework. They considered an ℓ_1-norm relaxation to solve this problem. It has been shown that the ℓ_1-norm relaxation can induce bias in location estimates [24].

A. Related Work

Modeling radio propagation indoors presents numerous challenges due to multipath interference, limited LoS paths, and site-specific variables. Various signal metrics, including Received Signal Strength (RSS), CSI, AoA, ToF, and Time-Difference-of-Arrival (TDoA), are used for indoor localization, each offering distinct advantages [2], [25], [26], [27], [28], [29].

Wi-Fi-based localization relies on technologies like IEEE 802.11, Bluetooth, ZigBee, RFID, and UWB, with IEEE 802.11 (Wi-Fi) being the most widely used. Wi-Fi networks serve as signal detection references, facilitating the creation of effective localization systems without additional infrastructure. However, improving localization accuracy requires sophisticated algorithms to overcome challenges such as unregulated interference and signal fluctuations [30], [31], [32].

Localization algorithms play a crucial role in localizing objects or individuals within an environment. Conventional methods include triangulation [33], Kalman filters [34], compressed sensing [1], multidimensional scaling [35], direct localization [36], and fingerprinting [37]. Learning-based methods, including supervised [38], unsupervised [39], semi-supervised [40], reinforcement [41], transfer [42], federated [43], and deep learning [44], offer more sophisticated approaches to localization, leveraging machine learning techniques for improved accuracy and efficiency.

Direct localization, as a technique within Wi-Fi-based localization, aims to enhance the accuracy and efficiency of positioning signal sources by directly calculating their locations without intermediate parameter estimations. This method has evolved significantly over time, with advancements such as the direct position determination (DPD) technique and the introduction of algorithms like direct location estimation (DLE) and Direct Source Localization (DiSouL) [19], [21], [22], [23].

Direct localization offers several advantages over traditional methods, including reduced computational complexity, faster localization process, and improved accuracy in challenging multipath environments. Despite facing challenges in wider-area networks and environmental characteristics, continued research and development are expected to further enhance the accuracy, efficiency, and applicability of direct localization methods [19], [23], [45].

B. Contributions and Organization

This paper proposes a novel direct localization method by co-processing the received signal at all antenna arrays. To co-process data, we take advantage of the fact that LoS path from the mobile user to all of the antenna arrays originates from a common location in the area. Nevertheless, non-LoS (NLoS) paths are caused by reflection from different objects in the environment, making them to have a random nature. In other words, when we grid the area, the strongest signal received at all the antenna arrays comes from one of the grid points. Taking this fact into account, the localization problem can be formulated as a sparse support recovery problem. Therefore, we employ a compressed sensing framework for our direct localization approach which is an NP-hard optimization problem. As mentioned before, ℓ_1-norm relaxation is generally used to make this problem tractable which results in inherent bias to the solution. However, recently, authors of [46] proposed that under some conditions, binary approximation for ℓ_0-norm optimization problems leads to optimal support. In addition, although the binary approximation is still NP-hard, there exists efficient binary programming solvers such as branch-and-bound methods and annealing-based methods.

In particular, we reformulate our problem as a binary ℓ_0-norm minimization problem inspired by [8]. In this paper, in order to solve this problem, we use annealing-based solvers. These solvers are able to solve optimization problems in the format of an Ising energy problem. Thus, we convert our problem to an Ising energy problem to be able to utilize recent efficient binary programming solvers. This research builds on initial ideas presented in [47], taking them further with a deep dive into the proposed method, thorough testing with real indoor data, and an in-depth statistical evaluation, including calculating the Cramér-Rao Bound (CRB) to compare with existing localization methods.

To summarize, the key contributions of our work are:

- Providing an in-depth explanation of using the Ising model to tackle direct localization problems, establishing a solid foundation for solving these problems.
- Determining specific conditions that allow our binary approximation method to accurately locate signal origins, improving the precision of localization.
- Conducting a statistical efficiency assessment with the CRB, offering insights into the reliability and precision of the method.
- Supporting our theoretical insights with real-world tests, comparing the performance of our proposed method with other existing approaches.

Ultimately, this paper seeks to advance the field of direct localization by merging theoretical insights with practical tests, aiming for localization solutions that are both more accurate and efficient.

In the present paper, we first provide a detailed explanation of the method proposed in [47]. Furthermore, we extend the study of the performance and robustness of our method on experimental data collected in a typical indoor environment. Additionally, we further analyze the statistical efficiency of our method by deriving the *Crámer-Rao Bound (CRB)* and compare its performance with the existing methods in the literature.

To summarize, our main contributions in this paper are as follows:

- We derive the details of the Ising model for the direct localization problem;
- We propose the conditions under which our binary approximation leads the accurate signal support;
- We analyze the statistical efficiency of our method by deriving the CRB;
- We provide additional experimental results in real environments for the performance of our method compared to some of the existing methods in literature in real environments.

The rest of the paper is organized as follows. Section II introduces our system model. In Section III, we explain our methodology and formulations in detail. In Section IV, we derive CRB for our method and compare the performance of our method and [23] with CRB. The experimental performance of our method and its comparison to the existing literature is given in Section V. Finally, Section VII concludes the paper.

II. System Model

Consider a multipath indoor environment, where P access points receive the narrow-band signal emitted from a nearfield WiFi user. Each access point is equipped with a uniform linear antenna array (ULA) with M elements. The pth access point is placed at $[\tilde{x}_a^p, \tilde{y}_a^p, \tilde{z}_a^p]^T$. The source is equipped with an omnidirectional antenna and is located at $[\tilde{x}_u, \tilde{y}_u, \tilde{z}_u]^T$. For the simplicity of discussion, we assume that the source and all the access points are located at the same height, i.e.

$$\tilde{z} = \tilde{z}_u = \tilde{z}_a^p, \ p = 1, 2, \cdots, P.$$

With this assumption, our scenario is reduced to a two-dimensional multipath case, and we need to estimate $\tilde{x}_u$ and $\tilde{y}_u$. Extension of our method to three-dimensional scenarios is straightforward.

The source transmits a signal. This signal propagates through the multipath environment and is received by all access points. The $M \times 1$ received signal vector arriving at access point p with the angle θ_p and in the range r_p from the access point p in one snapshot, $\mathbf{y}_p$, is given by:

$$\mathbf{y}_p = \sum_{l=1}^{L} \mathbf{a}(\theta_p^l, r_p^l) s_p^l + \mathbf{n}_p \tag{1}$$

where L is the nmber of paths, $s_p^l \in \mathbb{C}$ is a scalar that represents the complex signal amplitude in the multipath environment, $\mathbf{n}_p \in \mathbb{C}^{M\times 1}$ is the complex white Gaussian noise vector, and $\mathbf{a}(\theta_p^l, r_p^l) \in \mathbb{C}^{M\times 1}$ is the complex array manifold vector, which for a ULA positioned in the vicinity of a nearfield source is formulated as

$$\mathbf{a}(\theta_p, r_p) = \left[1, \Gamma_{\theta_p, r_p}^{(1)}, \cdots, \Gamma_{\theta_p, r_p}^{(M-1)}\right]^T \tag{2}$$

with

$$\Gamma_{\theta_p, r_p}^{(m)} = e^{-jm2\pi \frac{d}{\lambda} \sin(\theta_p) + jm^2 \frac{\pi d^2}{\lambda r_p} \cos^2(\theta_p)} \tag{3}$$

where θ_p is the AoA of the wave impinging on the pth access point, r_p is the distance between the source and the pth access point, d is the distance between two adjacent elements of the array, and λ is the wavelength.

In (1), $\mathbf{y}_p$ is measured and known and $\mathbf{n}_p \sim \mathcal{CN}(0, \sigma^2\mathbf{I})$, where $\mathbf{I}$ is the $M \times M$ identity matrix. In addition, s_p^l, θ_p^l, and r_p^l are unknown parameters and should be estimated. Note that θ_p^1 and r_p^1 represent the LoS path and are geometrically related to the location of the source. To be more specific:

$$\theta_p^1 = \arctan\left(\frac{\tilde{y}_a^p - \tilde{y}_u}{\tilde{x}_a^p - \tilde{x}_u}\right) + \frac{\pi}{2} - \pi I(\tilde{x}_u < \tilde{x}_a^p) \tag{4}$$

where $I(.)$ is the identity function and

$$r_p^1 = \sqrt{(\tilde{y}_a^p - \tilde{y}_u)^2 + (\tilde{x}_a^p - \tilde{x}_u)^2} \tag{5}$$

The term $-\pi I(\tilde{x}_u < \tilde{x}_a^p)$ is added to resolve the ambiguity in the angles generated by arctan(.) (i.e., four quarters of the unit circle).

III. Methodology

In this part, we explain our methodology for localization, which is based on *Compressed Sensing*. Our method is based on the direct estimation of the location of the source. In other words, we grid the two-dimensional environment and utilize these grid points in our estimator. To increase the resolution of localization, we take advantage of co-processing the received signal at all the access points. In other words, we jointly estimate the AoA and range for all the access points, and throughout this process, the location of the user is directly estimated.

An important fact to consider is that the nature of the received signal is *sparse*. Empirical studies in indoor WiFi systems have validated the assumption of sparsity in signal representation, with observations indicating a limited number of dominant paths, typically around five [7]. This observation supports the notion that despite complex propagation environments, significant contributors to received signals are few enough to be considered sparse. To be more specific, the line-of-sight (LoS) components of the received signal for all the access points are consistent, i.e., the LoS paths for all the received signals originate from the location of the source. Nonetheless, this is not the case for the limited number of non-line-of-sight (NLoS) paths. In a multipath environment, NLoS paths are reflected from different objects in the environment, which causes a random nature for these NLoS paths. This fact helps us to use a compressed sensing structure for our method.

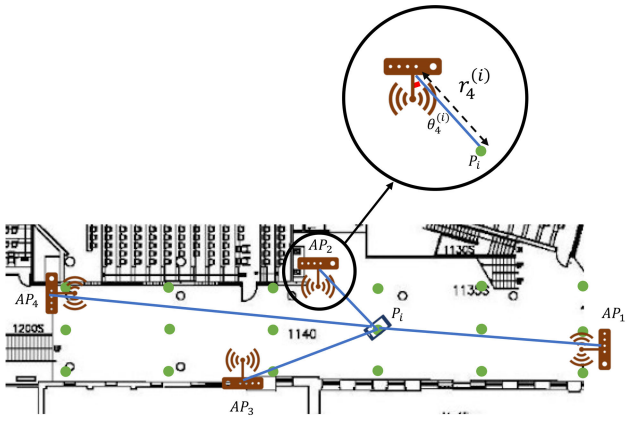

Fig. 1. A two-dimensional environment and an arbitrary grid over it.

In our method, we first grid our environment. Then, using the position information from our grid points, we form an over-complete array manifold to exploit compressed sensing. Next, we form our recovery problem, which is NP-hard. To solve this NP-hard problem, we restructure it into an Ising model.

A. Problem Formulation

Consider a grid over the environment, as shown in Fig. 1. The set of grid points is denoted by $\mathcal{S}$:

$$\mathcal{S} = \{\hat{\mathbf{p}}_1, \hat{\mathbf{p}}_2, \cdots, \hat{\mathbf{p}}_G\} \tag{6}$$

where G is the total number of grid points and $\hat{\mathbf{p}}_i = [\hat{x}^i, \hat{y}^i]^T$.

Now, assume the source is located at point $\hat{\mathbf{p}}_i \in \mathcal{S}$. As shown in Fig. 1, access point p measures the received signal from the source located at this point at the angle $\theta_p^{(i)}$ and with the range $r_p^{(i)}$. Using (4), the arriving angle is related to the position of the source by

$$\theta_p^{(i)} = \arctan\left(\frac{\hat{y}^i - \tilde{y}_p}{\hat{x}^i - \tilde{x}_p}\right) + \frac{\pi}{2} - \pi I(\hat{x}^i < \tilde{x}_p). \tag{7}$$

Also, considering (5), the range has the following relation with the position of the source

$$r_p^{(i)} = \sqrt{(\hat{y}^{(i)} - \tilde{y}_p)^2 + (\hat{x}^{(i)} - \tilde{x}_p)^2}. \tag{8}$$

Considering this grid, we can form an over-complete array manifold matrix for each access point:

$$\mathbf{\Psi}_p = [\mathbf{a}(\theta_p^{(1)}, r_p^{(1)}), \mathbf{a}(\theta_p^{(2)}, r_p^{(2)}), \cdots, \mathbf{a}(\theta_p^{(G)}, r_p^{(G)})] \tag{9}$$

where $\mathbf{a}(.)$ is defined in (2).

The measured received signal vector at access point p can be modeled as follows:

$$\mathbf{y}_p = \mathbf{\Psi}_p \mathbf{s}_p + \mathbf{n}_p \tag{10}$$

where $\mathbf{y}_p$ is the $M \times 1$ complex received signal, $\mathbf{s}_p$ is a $G \times 1$ complex vector of signal amplitudes for different grid points, $\mathbf{n}_p$ the $M \times 1$ vector of white Gaussian noise, $\mathbf{\Psi}_p$ is an $M \times G$ array manifold matrix.

As discussed in the previous section, $\mathbf{s}_p$ has a sparse nature. We assume that the user is located at one of those G grid points. Therefore, in an environment with no reflections, only one of the elements of $\mathbf{s}_p$ indicates LoS path is non-zero, and the rest are zero. However, in a multipath environment, the signal is reflected from the objects in the environment. The received signal is a combination of both the LoS path and the reflections of the transmitted signal. Therefore, $\mathbf{s}_p$ has multiple non-zero components.

Since the LoS paths of all the access points come from the location of the source, the element in $\mathbf{s}_p$ corresponding to the LoS path should be the same. Nevertheless, the NLoS paths stem from different locations in the environment; thus, they do not need to coincide.

To estimate the location of the user, we need to estimate $\mathbf{s}_p$ for each access point. An effective method to do that is to use compressed sensing. In the compressed sensing theory, a $G\times1$ sparse signal can be reconstructed with M measurements, where $G \gg M$ [16]. Then the joint signal recovery problem can be formed as follows:

$$\begin{aligned} \min_{\mathbf{s}_p} \quad & \sum_{p=1}^{P} ||\mathbf{s}_p||_0 \\ \text{s.t.} \quad & ||\mathbf{y}_p - \mathbf{\Psi}_p \mathbf{s}_p||_2^2 < \epsilon, \quad p = 1, 2, \cdots, P \end{aligned} \tag{11}$$

where ϵ is the maximum allowable mismatch between the observations and reconstructions.

This problem is NP-hard. To find a solution, the common methods are to either solve the problem with greedy methods or approximate it with a tractable problem [16]. However, in this paper, we solve the NP-hard problem using the binary approximation.

B. Binary Formulation

Consider a set of signals transmitted from the source and received by the receiver antenna arrays. These signals are taken as unit gain symbols. Therefore, the elements of the vector $\mathbf{s}_p$, which correspond to the gain of the transmitted signal at each grid point, will either be 0 or 1. Thus, we only need to estimate the support of our signals. So, (11) can be approximated with a binary program as

$$\begin{aligned} \min_{\mathbf{x}_p \in \{0,1\}^G} \quad & \sum_{p=1}^{P} ||\mathbf{x}_p||_0 \\ \text{s.t.} \quad & ||\mathbf{y}_p - \mathbf{\Psi}_p \mathbf{x}_p||_2^2 < \epsilon, \quad p = 1, 2, \cdots, P \end{aligned} \tag{12}$$

where $\mathbf{x}_p \in \{0, 1\}^G$ is a sparse $G\times1$ binary vector. This vector is the binary representation of $\mathbf{s}_p$. Thus, all the elements of $\mathbf{x}_p$ should be zero except the elements that correspond to the grid points that the signal emits from.

As discussed above, all the access points share the same LoS element $\mathbf{x}_p$ due to the fact that the mobile user is located on one of the grid points. Additionally, we are going to find the location of the user which can be identified if the LoS component is estimated. We approximate all the binary signal representations with the LoS component and therefore, we can omit the p index and use the $\mathbf{x}$ vector instead.

$$\begin{aligned} \min_{\mathbf{x} \in \{0,1\}^G} \quad & ||\mathbf{x}||_0 \\ \text{s.t.} \quad & ||\mathbf{y}_p - \mathbf{\Psi}_p \mathbf{x}||_2^2 < \epsilon, \quad p = 1, 2, \cdots, P \end{aligned} \tag{13}$$

It is essential to note that this binary approximation restricts the feasible set of our solution since $\mathbf{x}$ is a binary vector. Thus, the solution to this optimization problem is an upper bound to the exact solution.

In the process of transforming the original problem into a binary programming problem, as described in (13), it is important to note that there is no guarantee that the solutions for the original problem and the binary programming problem will share the same fundamental structure. A recent study, referenced in [46], demonstrated that subject to certain conditions on how the dictionary is constructed, approximating the solution of a binary programming problem like (13) with binary elements can indeed yield optimal support for the signal. These conditions require that the dictionary should be a tight frame and also satisfy the structural model of the system.

In practice, it is not guaranteed that the dictionary created based on arbitrary grid points will satisfy these conditions. For our case, we need a grid over the whole environment that is shared among all the access points. Thus, we create the over-complete manifold of all access points as follows:

$$\mathbf{\Psi} = \begin{bmatrix} \mathbf{\Psi_1} & 0 & \cdots & 0 \\ 0 & \mathbf{\Psi_2} & \cdots & 0 \\ \vdots & \vdots & \ddots & \vdots \\ 0 & 0 & \cdots & \mathbf{\Psi_P} \end{bmatrix} \tag{14}$$

in which $\mathbf{\Psi}_p$ is the array manifold of the p-th access point.

The construction of a tight frame requires two key conditions to be met:

- All eigenvalues should be equal, specifically G/M.
- The atom structure aligns with the proposed system model.

To achieve these conditions, an alternating projection algorithm, detailed in Algorithm 2 of [46], can be employed to design the grid. The Alternating Projections Grid Design is an iterative technique for direct location estimation. It starts by setting up initial grid points and then refines these points through iterations that balance between meeting spectral and structural requirements until the process converges or reaches a predefined number of cycles. Each iteration involves mathematical projections to satisfy specific matrix characteristics, such as maintaining a tight frame, and the grid points are adjusted accordingly to minimize the distance to these projections. The complexity of the algorithm is influenced by the computational tasks such as matrix operations and the number of grid points, which are vital for the precision and efficiency of the location estimates. Utilizing this grid design ensures that when addressing the binary program (13), the optimal support for the signal can be accurately attained.

C. Ising Energy Modeling

1) Definition of the Ising Model: The Ising energy model is a mathematical model proposed to describe the system of interaction between spins of atoms in statistical physics [48]. When the system is in its equilibrium state, its energy is minimum. The goal of this model is to reach the equilibrium state by minimizing the energy of the system given by

$$E(\mathbf{x}; \mathbf{b}, \mathbf{W}) = -\sum_{i=1}^{K} b_i x_i - \sum_{i=1}^{K} \sum_{j=1}^{K} W_{i,j} x_i x_j \tag{15}$$

where K is the number of binary states represented by $x_i \in \{-1, +1\}$, b_i shows the bias term and $W_{i,j}$ denotes the connection weight.

Although the Ising model is primarily a physical model, the description and formulation of its energy function introduced in (15) can be generalized to be used in different branches of mathematics such as graph theory, combinatorics, neural networks and so on [48].

For instance, in (15), the variable x_i represents the spin of atoms and has a binary value, which is originally considered to be $\{-1, +1\}$ to show the state of the spin. However, the Ising energy model can easily be converted to use $\{0, 1\}$ values. This conversion changes (15) to a *quadratic unconstrained binary optimization (QUBO)* problem, which is commonly used in Quantum computing [49].

2) Ising Model and QUBO: The *QUBO* structure is a robust framework that can be used to model several groups of optimization problems such as scheduling, graphs, etc., [50]. In addition, many NP-hard problems such as ℓ_0-norm optimization can be transformed into an Ising model [51]. Although QUBO problems and Ising model problems, such as (21), are NP-hard, their structure allows us to use efficient solvers, such as the quantum-based solvers, to find their solution [52]. Branch-and-bound based methods and annealing-based methods are among the common approaches to solving the QUBO problem.

Annealing-based solvers for Ising model problems usually take advantage of the Markov Chain Monte Carlo (MCMC) sampling methods. In the MCMC methods, a quantity or a distribution is approximated using randomly generated samples. Each sample depends only on its previous sample. The probability of transition between samples is designed so that in the steady state, the system approaches equilibrium. In the Ising model, the probability that the system is in the equilibrium state is given by

$$P(\mathbf{x}|\mathbf{b}, \mathbf{W}, \beta) = \frac{1}{Z(\mathbf{b}, \mathbf{W}, \beta)} exp(-\beta E(\mathbf{x}; \mathbf{b}, \mathbf{W})) \tag{16}$$

The probability given in (16) is the Gibbs or Boltzmann distribution. In (16), $\beta = 1/k_B T$, k_B is the Boltzman constant and T is the temperature. Also, $Z(\mathbf{b}, \mathbf{W}, \beta)$ is

$$Z(\mathbf{b}, \mathbf{W}, \beta) = \sum_{\mathbf{x}} exp(-\beta E(\mathbf{x}; \mathbf{b}, \mathbf{W})) \tag{17}$$

One of these sampling methods used in Ising models is the *Gibbs sampling*. In the Gibbs sampling, at each time, one of the spins is selected at random. Next, the probability of that spin being 1 or 0 is calculated given the current state of other spins and the temperature. The updated state of that spin is assigned to be 1 or 0 with their associated probabilities. This algorithm is repeated until it converges to the probability of equilibrium described in (16).

Another approach for the MCMC sampling, which is more efficient than the Gibbs sampling, is the *Metropolis-Hasting*

algorithm. In this approach, the energy change from flipping a randomly selected spin is considered, and the probability of accepting this change is calculated. If the energy change between the initial state and the new state is negative, we adopt this change by the probability of 1; otherwise, if it is positive, this energy is accepted with probability $exp(-\beta\Delta E)$. We iterate over this algorithm until its convergence to the equilibrium state distribution [48].

D. Ising Model Formulation

Problem (13) is a constrained binary optimization problem with a quadratic objective function. By doing some algebraic manipulations, this problem can be easily restructured into an Ising model problem.

We first modify (13) to a regularized minimization problem:

$$\min_{\mathbf{x}\in\{0,1\}^G} \quad ||\mathbf{x}||_0 + \gamma \sum_{p=1}^{P} ||\mathbf{y}_p - \mathbf{\Psi}_p\mathbf{x}||_2^2 \tag{18}$$

Next, we reframe (18) into an Ising energy model problem. In this case, we have G binary variables. We also need to calculate the bias and the connection weights of the variables. Since $x_i \in \{0, 1\}$, we have

$$||\mathbf{x}||_0 = \sum_{i=1}^{G} x_i. \tag{19}$$

Moreover, we can rewrite the second term in (18) as follows:

$$\begin{aligned}
&\sum_{p=1}^{P} ||\mathbf{y}_p\ \mathbf{\Psi}_p\mathbf{x}||_2^2 \\
&\quad= \sum_{p=1}^{P} (\mathbf{y}_p - \mathbf{\Psi}_p\mathbf{x})^H(\mathbf{y}_p - \mathbf{\Psi}_p\mathbf{x}) \\
&\quad= \sum_{p=1}^{P} \mathbf{y}_p^H\mathbf{y}_p - \mathbf{y}_p^H\mathbf{\Psi}_p\mathbf{x} - \mathbf{x}^H\mathbf{\Psi}_p^H\mathbf{y}_p + \mathbf{x}^H\mathbf{\Psi}_p^H\mathbf{\Psi}_p\mathbf{x} \\
&\quad= \sum_{p=1}^{P} ||\mathbf{y}_p||_2^2 - 2\Re(\mathbf{y}_p^H\mathbf{\Psi}_p\mathbf{x}) + \mathbf{x}^H\mathbf{\Psi}_p^H\mathbf{\Psi}_p\mathbf{x}
\end{aligned} \tag{20}$$

where $\Re(.)$ represents the real part of the expression.

Now, let us rewrite (18) as an Ising energy model using (19) and (20). We should also consider that when $x_i \in \{0, 1\}$, $x_i^2 = x_i$:

$$\begin{aligned}
\min_{\mathbf{x}\in\{0,1\}^G} &\sum_{i=1}^{G}(1 - \gamma \sum_{p=1}^{P}\sum_{m=1}^{M} 2\Re(y_{p,m}^H\Psi_{p_{m,i}} + \Psi_{p_{m,i}}^2))x_i \\
&+ \sum_{i=1}^{G}\sum_{j=1,j\neq i}^{G}\sum_{p=1}^{P}\sum_{m=1}^{M} \gamma\Psi_{p_{m,i}}^H\Psi_{p_{m,j}}x_ix_j.
\end{aligned} \tag{21}$$

So, based on (21), the bias term of the Ising formulation is:

$$\begin{aligned}
b_i = -1 + \gamma \sum_{p=1}^{P}\sum_{m=1}^{M} 2\Re(y_{p,m}^H\Psi_{p_{m,i}} + \Psi_{p_{m,i}}^2), \\
i = 1, 2, \ldots, G.
\end{aligned} \tag{22}$$

Furthermore, the connection weight is:

$$\begin{aligned}
W_{i,j} = \sum_{p=1}^{P}\sum_{m=1}^{M} \gamma\Psi_{p_{m,i}}^H\Psi_{p_{m,j}}, \\
i = j = 1, 2, \ldots, G, i \neq j.
\end{aligned} \tag{23}$$

To solve the above Ising model problem, we use an MCMC-based solver called the *Fujitsu Computing as a Service Digital Annealer* (DA) [53]. DA is a computer architecture that solves binary combinatorial problems with an Ising energy formulation as its objective function. According to [54], the time-to-solution of DA for the fully connected spin-glass problems has been about two times faster than the existing annealing and parallel tempering methods.

As we discussed in Section III-C, the Ising model represents the magnetic interaction between spins of a lattice and is described by the *Hamiltonian energy* as shown in (15). The model is based on the statistical mechanics. In the Ising model, we have a configuration of spins, c, and the energy of this configuration, $E(c)$, is described by (15). The probability of the system being in configuration c is related to this energy; in other words, $P(c) \sim \exp(-\beta E(c))$ where β is a constant. Then, considering the MCMC algorithms such as *Metropolis-Hastings*, we need to find the acceptance rate of the configurations, which depends on the difference between the energy of the configuration with a spin flip and its current state. So, the computational complexity of the whole system depends on the size of the connection weight matrix $\mathbf{W}$ and the bias vector $\mathbf{b}$. Thus, having G binary variables in our model, the computational complexity of our algorithm is of the order $O(G^2)$.

IV. Crámer-Rao Bound Derivation

In this section, we study the theoretical performance of our method by deriving CRB. CRB provides a common baseline for comparing the performance of unbiased estimators. Estimators whose performance is closer to the CRB have less bias and, therefore, preferable to use.

A. Derivation of CRB

In this section, we derive the CRB of the localization error for the signal model given by (10). First, let us define the vector of parameters:

$$\bar{\boldsymbol{\eta}} = [\tilde{x}_u, \tilde{y}_u]^T \tag{24}$$

where $\tilde{x}_u$ and $\tilde{y}_u$ represent the coordinates of the location of the user. The likelihood function of the received signal measurements at access point p in (10) is given by

$$f(\mathbf{y}_p|\bar{\boldsymbol{\eta}}) = \frac{1}{\det(2\pi\mathbf{\Sigma}_p)^{\frac{M}{2}}} \exp -(\mathbf{y}_p - \mu_p(\bar{\boldsymbol{\eta}}))^H\mathbf{\Sigma}_p^{-1}(\mathbf{y}_p - \mu_p(\bar{\boldsymbol{\eta}})) \tag{25}$$

in which $\mathbf{\Sigma}_p$ is the covariance matrix and $\mu_p(\bar{\boldsymbol{\eta}})$ is the mean vector and is defined as follows:

$$\mu_p(\bar{\boldsymbol{\eta}}) = \mathbf{\Psi}_p(\bar{\boldsymbol{\eta}})\bar{\mathbf{x}} = \sum_{i=1}^{G} \mathbf{a}(\theta_p^{(i)}(\bar{\boldsymbol{\eta}}), r_p^{(i)}(\bar{\boldsymbol{\eta}}))x_i \tag{26}$$

where $\mathbf{a}(.)$ is the steering vector defined in (2).

Given that the received signal measurements across all the access points are independent, the joint likelihood function for these measurements is given by

$$f(\mathbf{y}_1, \mathbf{y}_2, \cdots, \mathbf{y}_P|\bar{\boldsymbol{\eta}}) = \prod_{p=1}^{P} f(\mathbf{y}_p|\bar{\boldsymbol{\eta}}). \tag{27}$$

The log-likelihood function, $\mathcal{L}_{\mathbf{y}}(\bar{\boldsymbol{\eta}})$, can be found by taking the natural logarithm of (25) as

$$\mathcal{L}_{\mathbf{y}}(\bar{\boldsymbol{\eta}}) = \sum_{p=1}^{P} \ln f(\mathbf{y}_p|\bar{\boldsymbol{\eta}}). \tag{28}$$

We need to calculate the Fisher information matrix (FIM) to find the CRB. The FIM is the covariance of the derivative of the log-likelihood function with respect to the variables. The FIM is given by:

$$\begin{aligned}\mathbf{J}(\bar{\boldsymbol{\eta}}) &= E\{\nabla_{\bar{\boldsymbol{\eta}}}\mathcal{L}_{\mathbf{y}}(\bar{\boldsymbol{\eta}})\nabla_{\bar{\boldsymbol{\eta}}}\mathcal{L}_{\mathbf{y}}(\bar{\boldsymbol{\eta}})^H\} \\ &= -E\{\nabla_{\bar{\boldsymbol{\eta}}}\nabla_{\bar{\boldsymbol{\eta}}}^H\mathcal{L}_{\mathbf{y}}(\bar{\boldsymbol{\eta}})\}\end{aligned} \tag{29}$$

where $\nabla_{\bar{\boldsymbol{\eta}}} = [\partial/\partial\tilde{x}_u, \partial/\partial\tilde{y}_u]^T$. In this case, the matrix $\mathbf{J}(\bar{\boldsymbol{\eta}})$ is a 2×2 matrix with the following form:

$$\mathbf{J}(\bar{\boldsymbol{\eta}}) = \begin{bmatrix} J_{\tilde{x}_u\tilde{x}_u} & J_{\tilde{x}_u\tilde{y}_u} \\ J_{\tilde{y}_u\tilde{x}_u} & J_{\tilde{y}_u\tilde{y}_u} \end{bmatrix}. \tag{30}$$

Next, we derive each element of the matrix $\mathbf{J}(\bar{\boldsymbol{\eta}})$. Assume that the covariance of the noise across all access points is the same. To be more specific, $\Sigma_p = \Sigma = \sigma^2\mathbf{I}, p = 1, 2, \cdots, P$. Therefore, the second derivative of $\mathcal{L}_{\mathbf{y}}(\bar{\boldsymbol{\eta}})$ with respect to $\bar{\eta}_k$ and $\bar{\eta}_l$ is given by:

$$J_{k,l} = -E\Big\{\frac{\partial^2}{\partial\bar{\eta}_k\bar{\eta}_l}\mathcal{L}_{\mathbf{y}}(\bar{\boldsymbol{\eta}})\Big\} = \frac{2}{\sigma^2}\sum_{p=1}^{P}\Re\Big\{\frac{\partial\mu_p^H(\bar{\boldsymbol{\eta}})}{\partial\bar{\eta}_k}\frac{\partial\mu_p(\bar{\boldsymbol{\eta}})}{\partial\bar{\eta}_l}\Big\}. \tag{31}$$

Based on (31), we can define each element of FIM as follows. Note that θ_p^* and r_p^* are the estimated AoA and the range of the p-th access point from the estimated location of the user, $\bar{\boldsymbol{\eta}}$:

$$\begin{aligned}J_{\tilde{x}_u\tilde{x}_u} = \frac{2}{\sigma^2}\sum_{p=1}^{P}(\pi\frac{d}{\lambda r_p^{*2}}\cos\theta_p^*)^2\sum_{m=0}^{M-1}[2(\tilde{y}_u-\tilde{y}_p)m \\ + \frac{d}{r_p^*}(\tilde{y}_u-\tilde{y}_p)\sin\theta_p^*m^2 - \frac{d}{r_p^*}(\tilde{x}_u-\tilde{x}_p)\cos\theta_p^*m^2]^2,\end{aligned} \tag{32}$$

$$\begin{aligned}J_{\tilde{x}_u\tilde{y}_u} = J_{\tilde{y}_u\tilde{x}_u} = -\frac{2}{\sigma^2}\sum_{p=1}^{P}(\pi\frac{d}{\lambda r_p^{*2}}\cos\theta_p^*)^2\sum_{m=0}^{M-1}[2(\tilde{y}_u-\tilde{y}_p)m \\ + \frac{d}{r_p^*}(\tilde{y}_u-\tilde{y}_p)\sin\theta_p^*m^2 - \frac{d}{r_p^*}(\tilde{x}_u-\tilde{x}_p)\cos\theta_p^*m^2] \\ \times[2(\tilde{x}_u-\tilde{x}_p)m + \frac{d}{r_p^*}(\tilde{x}_u-\tilde{x}_p)\sin\theta_p^*m^2 \\ + \frac{d}{r_p^*}(\tilde{y}_u-\tilde{y}_p)\cos\theta_p^*m^2],\end{aligned} \tag{33}$$

$$\begin{aligned}J_{\tilde{y}_u\tilde{y}_u} = \frac{2}{\sigma^2}\sum_{p=1}^{P}(\pi\frac{d}{\lambda r_p^{*2}}\cos\theta_p^*)^2\sum_{m=0}^{M-1}[2(\tilde{x}_u-\tilde{x}_p)m \\ + \frac{d}{r_p^*}(\tilde{x}_u-\tilde{x}_p)\sin\theta_p^*m^2 + \frac{d}{r_p^*}(\tilde{y}_u-\tilde{y}_p)\cos\theta_p^*m^2]^2.\end{aligned} \tag{34}$$

The details of the derivations of these elements are given in Appendix A. Then, the CRB of the localization error is given by

$$CRB = \mathrm{tr}(\mathbf{J}^{-1}(\bar{\boldsymbol{\eta}})) = J_{11}^{-1} + J_{22}^{-1} \tag{35}$$

where J_{11}^{-1} and J_{22}^{-1} are the diagonal elements of the inverse of the FIM and are given by:

$$J_{11}^{-1} = \frac{J_{\tilde{y}_u\tilde{y}_u}}{J_{\tilde{x}_u\tilde{x}_u}J_{\tilde{y}_u\tilde{y}_u} - J_{\tilde{x}_u\tilde{y}_u}J_{\tilde{x}_u\tilde{y}_u}} \tag{36}$$

and

$$J_{22}^{-1} = \frac{J_{\tilde{x}_u\tilde{x}_u}}{J_{\tilde{x}_u\tilde{x}_u}J_{\tilde{y}_u\tilde{y}_u} - J_{\tilde{x}_u\tilde{y}_u}J_{\tilde{x}_u\tilde{y}_u}}. \tag{37}$$

Theorem 1: For $M \gg 1$, the CRB can be approximated by the following equation:

$$CRB \approx \frac{3\sigma^2\lambda^2}{10\pi^2 M}\Big(\frac{\sum_{p=1}^{P}(\frac{\cos\theta_p^*}{r_p^*})^2}{g(\theta_1^*, \theta_2^*, \cdots\theta_P^*, r_1^*, \cdots, r_P^*)}\Big) \tag{38}$$

where

$$\begin{aligned}&g(\theta_1^*, \theta_2^*, \cdots\theta_P^*, r_1^*, \cdots, r_P^*) \\ &= \sum_{p=1}^{P}\sum_{q=1}^{P}(\frac{\cos\theta_p^*\cos\theta_q^*}{r_p^*r_q^*})^2(4\sin^2\theta_q^*\cos^2\theta_p^* - \sin 2\theta_p^*\sin 2\theta_q^*)\end{aligned} \tag{39}$$

Proof: The proof is given in Appendix B. □

According to (38), the CRB of the localization error decreases with increasing SNR and also by increasing the number of antenna elements. We should also consider that $0 \le \cos\theta_p^* \le 1, p = 1, 2, \cdots, P$. Thus, we have the following corollary.

Corollary 1: Among the P access points, the one closer to the source will contribute more to the localization error.

The Corollary 1 is a direct result of Theorem 1. To elaborate further, Equation (38) exhibits an inverse relationship with the distance between the source and the access points.

V. Performance Evaluation

In this part, we evaluate the performance of our method by comparing it to other benchmarks in the literature. In our method, which we call ℓ_0-CS DLE, we provide a binary relaxation for the compressed sensing-based cooperative direct localization and use the DA to solve the problem. All experiments were conducted on the DA environment prepared for the research use. Note that other QUBO solvers can be used to solve this problem. We first demonstrate the experimental setup and then provide the performance evaluation for the simulated environment and the real environment data.

The first method, ℓ_1-CS DLE, that we use as a benchmark is proposed in [23]. In this method, authors designed a compressed sensing-based algorithm to estimate the location of the user in a multipath environment. The proposed technique jointly processes the received data at each access point and

estimates the location of the user without directly estimating LoS AoA. The authors used an ℓ_1-norm relaxation to transform the NP-hard compressed sensing problem into a second-order cone programming problem.

The second benchmark we are considering is a maximum likelihood direct location estimation (ML-DLE) proposed in [22]. In this method, the authors came up with a simple method that utilizes maximum-likelihood estimation over the grid to directly estimate the location of the source in a multipath environment. They compute the likelihood of the received signal at each access point given the known values of the AoA and ToA on a grid point. This algorithm needs statistical channel knowledge.

We also compared our method with the traditional maximum-likelihood-based indirect location estimation method (ML-ILE) [55]. In this method, first, the AoA of the received signal at each access point is estimated using the maximum likelihood estimator. Next, the location of the user is evaluated with triangulation.

A. Experimental Setup

We use ASUS RT_AC86U routers with three antennas as our receiver access points. The ASUS RT_AC86U routers work in 2.4 GHz and support a $20MHz$ bandwidth. The distance between two adjacent antennas of an ASUS RT_AC86U router is 8.7 cm. These routers run IEEE802.11ac MU-MIMO protocol and are equipped with Nexmon CSI Extractor Tool [56] for gathering the CSI information. In addition, we use Raspberry Pi4 as our transmitter.

After setting up the routers and Raspberry Pi4 in the environment, we can start collecting CSI data. Our goal is to localize the Raspberry Pi4, which is associated with a network or a router. The Raspberry Pi4 sends ping packets at $100Hz$. These packets are collected by ASUS routers which are programmed in the monitor mode. The routers monitor the wireless channel and then extract and store the CSI from the packets transmitted by the Raspberry Pi4 as the packet capture (pcap) files. For each experiment, Raspberry Pi4 generates packets for 300 seconds.

We should note that the receivers and the transmitter are not synchronized. Therefore, the CSI phase is distorted by the carrier frequency offset (CFO) and symbol timing offset (STO). To compensate for these phase distortions, the linearity of the CSI phase across subcarriers can be removed [57]. This phase cleaning procedure does not affect the AoA estimates, while it leads to a bias on the ToF estimates.

B. Simulation Results

In this section, we study the performance of the proposed localization method by comparing it to the benchmarks. For these evaluations, we generate the received signal for each access point using WIM2 simulator [58]. The channel model used in this simulator is the WINNER II channel model. This model can produce different multipath scenarios, such as indoor and urban environments. The Winner II channel model, which is a geometry-based stochastic channel model designed to represent the effects of multipath propagation accurately.

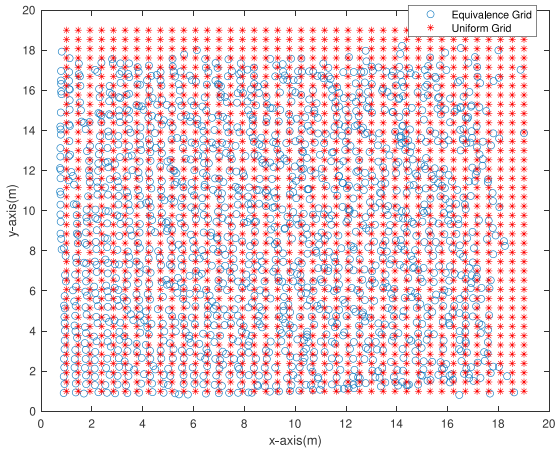

Fig. 2. The grid of size $G = 400$ designed based on Alternating projection algorithm.

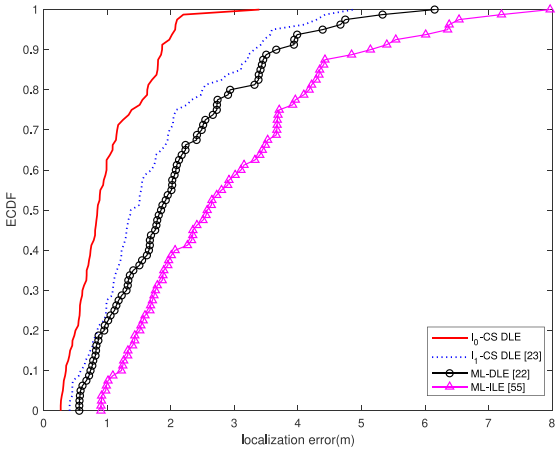

Fig. 3. ECDF of localization error for ℓ_0-CS DLE, ℓ_1-CS DLE [23], ML-DLE [22], and ML-ILE [55] for the simulated environment.

This model follows a statistical approach, capturing various channel parameters based on empirical distributions extracted from extensive measurement campaigns.

The Winner II channel model generates channel realizations by summing contributions from individual rays, each characterized by specific parameters including delay, power and angle-of-arrival. These parameters are stochastically determined, ensuring that the model captures the statistical variations observed in real-world propagation scenarios. Additionally, the model supports both LoS and NLoS conditions, making it suitable for indoor and outdoor environments alike.

For our simulations, we consider a $20m \times 20m$ area. In this area, three access points are located in the room with coordinates $[0m, 20m]$, $[20m, 15m]$, $[12m, 0m]$ and with orientations, $[0, 0, \frac{2\pi}{3}]$, $[0, 0, \frac{5\pi}{4}]$, $[0, 0, \frac{5\pi}{3}]$ with respect to the global coordinate system (GCS). The access points operate in 2.4 GHz and are equipped with a ULA with 10 elements. Within this space, the transmitter is located at $[7m, 8m]$, and 800 snapshots are collected for analysis. The non-uniform grid described in Section III that we used for building our dictionary is of size $G = 400$ and it is demonstrated in Fig. 2.

Fig. 3 compares the empirical cumulative distribution function (ECDF) of the localization error of the proposed method in this paper and the benchmarks. In this figure, the SNR is $20dB$. The median accuracy of our method, ℓ_0-CS DLE,

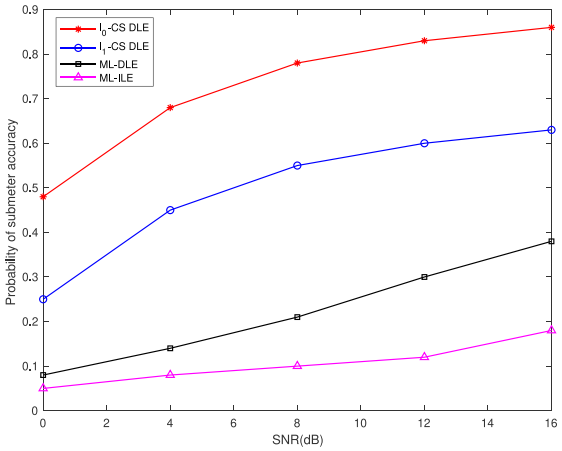

Fig. 4. Probability of submeter accuracy vs SNR for ℓ_0-CS DLE, ℓ_1-CS DLE [23], ML-DLE [22], and ML-ILE [55].

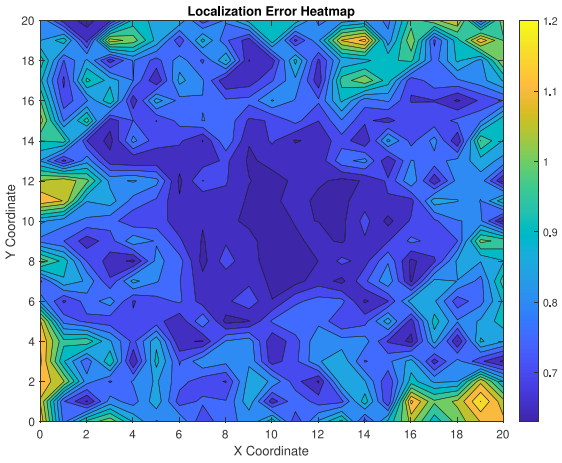

Fig. 5. Distribution of the localization error in the $20m \times 20m$ room.

is $0.32m$ while the median accuracy of ℓ_1-CS DLE, ML-DLE, and ML-ILE are $0.69m$, $1.21m$ and $1.76m$, respectively. To better understand Fig. 3, we study the probability of submeter accuracy with respect to increasing SNR. As presented in Fig. 4, by increasing SNR the received signal is more robust to noise. So, in all methods, the probability of sub-meter accuracy is enhanced with increasing SNR.

Moreover, Fig. 5 presents the distribution of localization errors within the simulated environment of the $20m \times 20m$ room. In constructing this figure, we computed the localization error for 100 distinct locations across the room and represented it as a heatmap. The depicted error distribution reveals a trend where proximity to the walls corresponds to increased error rates. This phenomenon is related to the intensified reflections from the walls, which adversely impact the accuracy of localization as objects approach the room boundaries.

C. Experimental Results

To further evaluate the performance of our method, we considered two different scenarios for our experiments. For these simulations, we also used the grid shown in Fig 2. The scenarios are shown in Fig. 6, and the details are discussed in the following sections:

1) Indoor Hall Scenario: In this scenario, we place the access points and the transmitter in a $40m \times 7m$ indoor hall. As shown in Fig. 6(c), we deploy four routers (determined by the red circles), and we consider one transmitter (determined by the green circle) to localize. The locations of the receivers and the transmitter are shown roughly in Fig. 6(a). In this scenario, we have some reflections from walls and some objects in the environment. We collected 800 snapshots for the location of the transmitter shown in Fig. 6(a).

Fig. 7 shows the comparison between the ECDF of ℓ_0-CS DLE and the three benchmarks, namely ℓ_1-CS DLE [23], ML-DLE [22], and ML-ILE [55]. In this scenario, the median accuracy of ℓ_0-CS DLE is around $0.64m$ while for ℓ_1-CS DLE is around $1.07m$, for ML-DLE is around $1.55m$ and for ML-ILE is around $2.04m$. The ℓ_0-CS DLE method had a median accuracy that was nearly 40% better than the ℓ_1-CS DLE method and was almost 58% and 68% better than the ML-DLE and ML-ILE methods, respectively.

2) Indoor Corridor Scenario: The scenario is set up in a $2.5m \times 30m$ corridor as shown in Fig. 6(d). As shown in Fig. 6(b), in this scenario, we deploy three access points (denoted by the red circles). The transmitter is denoted by a green circle) in the environment. For this scenario, we also gathered 800 snapshots for the position of the transmitter, as illustrated in Fig. 6(a). Because this environment is a narrow corridor, there are more reflections from the walls and the objects compared to the previous scenario.

Fig. 8 represents a comparison between the ECDF of ℓ_0-CS DLE, ℓ_1-CS DLE, ML-DLE, and ML-ILE for the indoor corridor scenario. In this scenario, the median error of ℓ_0-CS DLE, ℓ_1-CS DLE, ML-DLE, and ML-ILE are around $0.87m$, $1.3m$, $1.92m$, and $2.68m$, respectively. Due to stronger reflections, the error for all methods is higher in this scenario compared to the previous scenario. The median accuracy of the ℓ_0-CS DLE method was significantly improved compared to the ℓ_1-CS DLE method, as well as the ML-DLE and ML-ILE methods, by almost 33%, 54%, and 67%, respectively.

D. Overall Evaluation

In this section, we present an overall evaluation of our method compared to the benchmarks. We compare the processing time of all methods. In addition, we compare the performance of all methods in different scenarios. Moreover, we compared the derived CRB in Section. IV with the root mean squared error (RMSE) of localization.

Table. I presents the processing time of all four methods. For this comparison, we ran the program for each algorithm multiple times and considered the average of this timing. As represented in Table. I, ℓ_1-CS DLE has the highest processing time since in the second-order cone programming method, the number of variables to be determined is much more than our proposed method, and this will increase the time complexity. In addition, in the direct localization methods, the processing time is higher than in the indirect methods because of the joint processing of the received signal at all the access points.

In Fig. 9, we compare the performance of the methods in 3 different scenarios by plotting the bar graph of the average localization error for all benchmarks. Two of the scenarios are shown in Fig. 6. We also considered the case study where in

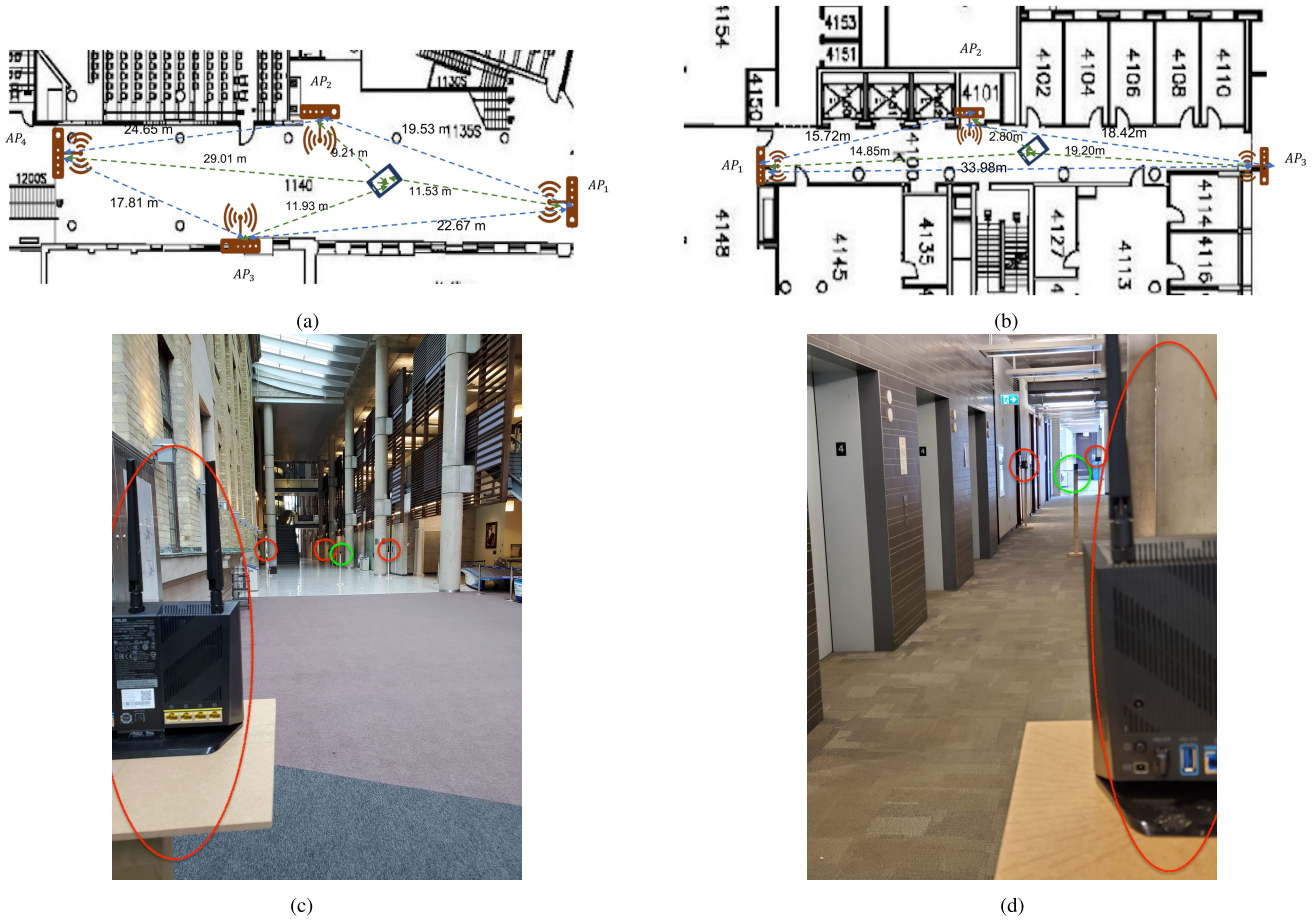

Fig. 6. (a) Indoor hall scenario map; (b) indoor corridor scenario map; (c) indoor hall; (d) indoor corridor.

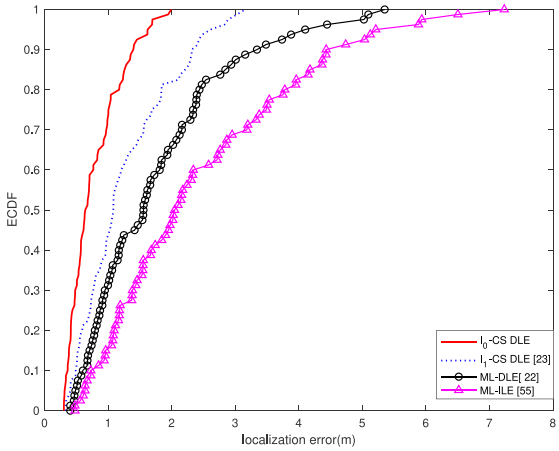

Fig. 7. ECDF of localization error for (ℓ_0-CS DLE, ℓ_1-CS DLE [23], ML-DLE [22], and ML-ILE [55] for the indoor hall scenario.

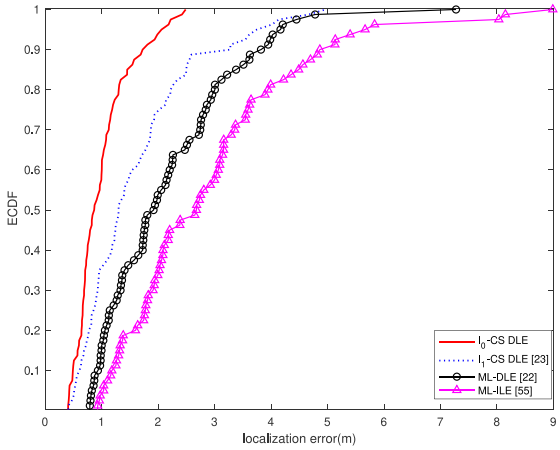

Fig. 8. ECDF of localization error for ℓ_0-CS DLE, ℓ_1-CS DLE [23], ML-DLE [22], and ML-ILE [55] for the indoor corridor scenario.

the same indoor hall shown in Fig. 6(c), we have 3 access points instead of 4. We should note that the localization error depends on multiple environmental parameters, such as the number of access points, the environment, etc. As noticed in Fig. 9, the average localization error for all the benchmarks is lower in the indoor hall compared to the indoor corridor. The reason for this observation is that the geometry of the hall provides fewer reflections compared to the indoor corridor. In addition, when we have fewer access points in the same geometry, the average localization error is higher.

Finally, in Fig. 10, we compare the derived CRB in Section. IV with the RMSE of localization for all benchmarks with respect to SNR for the simulated scenario discussed in Section V-B. Fig. 10 shows that as SNR increases, the RMSE of localization for our method gets closer to CRB. In addition, our proposed method has a closer RMSE to CRB.

VI. Limitations and Future Work

While our proposed localization approach represents a significant advancement in indoor environments, it is important to

TABLE I
COMPARISON OF THE AVERAGE PROCESSING TIME OF ℓ_0-CS DLE, ℓ_1-CS DLE [23], ML-DLE [22], AND ML-ILE [55]

Method	Processing time (ms)
ℓ_0-CS DLE	79
ℓ_1-CS DLE [23]	2.1×10^3
ML-DLE [22]	67
ML-ILE [55]	33

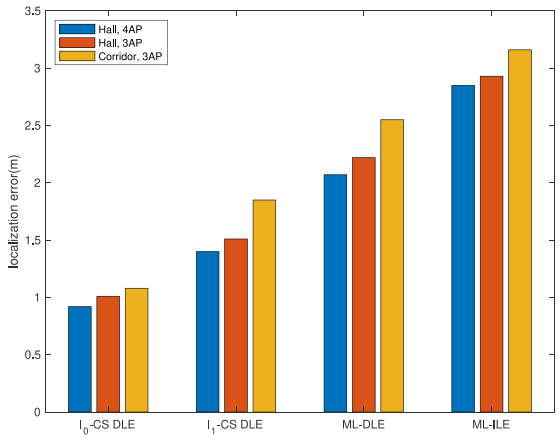

Fig. 9. Comparison of the average Localization error for all methods (ℓ_0-CS DLE, ℓ_1-CS DLE [23], ML-DLE [22], and ML-ILE [55]) in different scenarios.

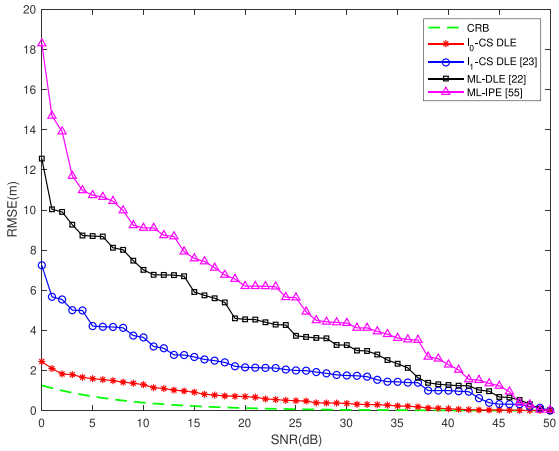

Fig. 10. RMSE performance comparison for localization methods (ℓ_0-CS DLE, ℓ_1-CS DLE [23], ML-DLE [22], and ML-ILE [55]) as a function of SNR.

acknowledge several limitations that may impact its practical deployment. Furthermore, there are opportunities for future research to address these limitations and further enhance the effectiveness of the system.

Firstly, the scenarios considered in this study are predominantly static, with the Raspberry Pi transmitting pings at a fixed rate of 100Hz, and data being collected over a period of 300 seconds. Similarly, simulated scenarios are also static. However, real-world deployments often involve mobile nodes, leading to dynamic changes in the environment. Future research could delve into evaluating the performance of the system under dynamic scenarios and explore achievable update rates when nodes are in motion.

Secondly, the robustness of the localization algorithm may be compromised in scenarios where the LoS to one of the access points is obstructed by obstacles or environmental factors. To address this, future research could explore methods to enhance the robustness of the algorithm. This may involve incorporating redundancy or adaptive mechanisms to detect and mitigate the impact of LoS loss. Additionally, while our work primarily focuses on detecting LoS, the simplifying assumption neglects the effects of NLoS paths. Future research could consider integrating the structure of NLoS or the geometry of the environment to reduce the ambiguity caused by the reflections.

In addition, expanding the proposed approach to 3D scenarios is straightforward from a geometric perspective. The current methodology relies on estimating the angle of arrival (θ_p) and range (r_p) parameters, which are geometrically tied to the location of the source. Extending this to three dimensions involves adding an additional coordinate (elevation angle) for the position of the source. In a 3D scenario, estimating the position of the source entails considering both horizontal ($\tilde{x}_u$ and $\tilde{y}_u$) and vertical ($\tilde{z}_u$) components. However, the estimation process would likely follow similar principles as outlined for the 2D case, involving angle calculation and range estimation.

The complexity of extending the approach to 3D scenarios depends on various factors. Adapting the localization algorithm to handle 3D coordinates requires modifications to account for the added dimensionality. This could increase the computational load to a polynomial order, particularly for larger numbers of access points (P) or antenna array elements (M). Moreover, incorporating the vertical component of received signals may necessitate additional data processing. While the geometric transition to 3D is straightforward, the algorithmic and computational complexities must be carefully addressed for efficiency in three-dimensional environments. These aspects warrant consideration for future research endeavors.

Moreover, Table I provides insights into the relative processing power required for the proposed localization method. Future work could concentrate on optimizing the algorithm for reduced computational complexity. This optimization would enable deployment on resource-constrained devices commonly used in wireless networks.

In conclusion, although our proposed localization system shows promise for indoor deployments, addressing the outlined limitations and exploring future research avenues will be crucial to realize its full potential in practical applications.

VII. CONCLUSION

This paper introduces an innovative approach for direct localization in a multipath environment with multiple access points. In this method, we simultaneously process the received signals from all available access points. This problem is framed as a compressed sensing problem which we then transform into an Ising model representation. The Ising model, constituting a quadratic unconstrained binary optimization

problem, is solved through Markov Chain Monte Carlo (MCMC) methods. To assess the performance and efficacy of our proposed method, we conduct experiments in distinct scenarios by gathering data under diverse conditions. Our comprehensive analysis of the outcomes demonstrates that the approach presented in this paper significantly outperforms existing methods documented in the current literature. Our findings highlight the potential of the proposed Ising model-based technique for direct localization in multipath environments with multiple access points.

APPENDIX A
DETAILS OF THE DERIVATION OF CRB

Consider the user is located on the grid point g^*. Then the vector $\mathbf{x}$ has a 1 at its g^*-th element, and the other elements are zero. Thus,

$$\mu_p(\bar{\boldsymbol{\eta}}) = \mathbf{a}(\theta_p^{(g^*)}(\bar{\boldsymbol{\eta}}), r_p^{(g^*)}(\bar{\boldsymbol{\eta}})). \tag{40}$$

According to (31), we need to calculate the first derivative of $\mu_p(\bar{\boldsymbol{\eta}})$ with respect to the elements of $\bar{\boldsymbol{\eta}}$ which are $\tilde{x}_u$ and $\tilde{y}_u$:

$$\frac{\partial \mu_p(\bar{\boldsymbol{\eta}})}{\partial \tilde{x}_u} = \frac{\partial \mu_p(\bar{\boldsymbol{\eta}})}{\partial \theta_p^{(g^*)}(\bar{\boldsymbol{\eta}})}\frac{\partial \theta_p^{(g^*)}(\bar{\boldsymbol{\eta}})}{\partial \tilde{x}_u} + \frac{\partial \mu_p(\bar{\boldsymbol{\eta}})}{\partial r_p^{(g^*)}(\bar{\boldsymbol{\eta}})}\frac{\partial r_p^{(g^*)}(\bar{\boldsymbol{\eta}})}{\partial \tilde{x}_u} \tag{41}$$

and

$$\frac{\partial \mu_p(\bar{\boldsymbol{\eta}})}{\partial \tilde{y}_u} = \frac{\partial \mu_p(\bar{\boldsymbol{\eta}})}{\partial \theta_p^{(g^*)}(\bar{\boldsymbol{\eta}})}\frac{\partial \theta_p^{(g^*)}(\bar{\boldsymbol{\eta}})}{\partial \tilde{y}_u} + \frac{\partial \mu_p(\bar{\boldsymbol{\eta}})}{\partial r_p^{(g^*)}(\bar{\boldsymbol{\eta}})}\frac{\partial r_p^{(g^*)}(\bar{\boldsymbol{\eta}})}{\partial \tilde{y}_u} \tag{42}$$

Now, we need to calculate each of the partial derivatives in (41) and (42). For the simplicity of notation, we omit the dependence of $\theta_p^{(g^*)}(\bar{\boldsymbol{\eta}})$ and $r_p^{(g^*)}(\bar{\boldsymbol{\eta}})$ to $\bar{\boldsymbol{\eta}}$ and (g^*) and show them by θ_p^* and r_p^*:

$$\frac{\partial \mu_p(\bar{\boldsymbol{\eta}})}{\partial \theta_p^*} = [da_{\theta_p^*,0}, da_{\theta_p^*,1}, \cdots, da_{\theta_p^*,(M-1)}]^T \tag{43}$$

where

$$da_{\theta_p^*,m} = -j2\pi\frac{d}{\lambda}m\cos\theta_p^*(1 + m\frac{d}{r_p^*}\sin\theta_p^*)\Gamma_{\theta_p^*, r_p^*}{}^{(m)}$$

and $\Gamma^{(m)}_{\theta_p^*, r_p^*}$ is defined in (3).

$$\frac{\partial \mu_p(\bar{\boldsymbol{\eta}})}{\partial r_p^*} = [da_{r_p^*,0}, da_{r_p^*,1}, \cdots, da_{r_p^*,(M-1)}]^T \tag{44}$$

in which

$$da_{r_p^*,m} = -j\pi\frac{d^2}{\lambda r_p^{*2}}m^2\cos^2\theta_p^*\Gamma^{(m)}_{\theta_p^*, r_p^*}.$$

Based on (7), we can find the partial derivative of θ_p^* with respect to $\tilde{x}_u$ and $\tilde{y}_u$:

$$\frac{\partial \theta_p^*}{\partial \tilde{x}_u} = -\frac{(\tilde{y}_u - \tilde{y}_p)}{r_p^{*2}} \tag{45}$$

and

$$\frac{\partial \theta_p^*}{\partial \tilde{y}_u} = \frac{(\tilde{x}_u - \tilde{x}_p)}{r_p^{*2}} \tag{46}$$

Similarly, using (8), we can calculate partial derivative of r_p^* with respect to $\tilde{x}_u$ and $\tilde{y}_u$:

$$\frac{\partial r_p^*}{\partial \tilde{x}_u} = \frac{(\tilde{x}_u - \tilde{x}_p)}{r_p^*} \tag{47}$$

and

$$\frac{\partial r_p^*}{\partial \tilde{y}_u} = \frac{(\tilde{y}_u - \tilde{y}_p)}{r_p^*}. \tag{48}$$

Next, we substitute all the partial derivatives into (41) and (42). $[.]_m$ represents the m-th element of of the $M\times 1$ vector of the partial derivatives:

$$\begin{aligned}\left[\frac{\partial \mu_p(\bar{\boldsymbol{\eta}})}{\partial \tilde{x}_u}\right]_m &= j\pi\frac{d}{\lambda r_p^{*2}}\cos\theta_p^*[2(\tilde{y}_u - \tilde{y}_p)m \\ &+ \frac{d}{r_p^*}(\tilde{y}_u - \tilde{y}_p)\sin\theta_p^* m^2 - \frac{d}{r_p^*}(\tilde{x}_u - \tilde{x}_p)\cos\theta_p^* m^2]\Gamma^{(m)}_{\theta_p^*, r_p^*},\end{aligned} \tag{49}$$

and

$$\begin{aligned}\left[\frac{\partial \mu_p(\bar{\boldsymbol{\eta}})}{\partial \tilde{y}_u}\right]_m &= -j\pi\frac{d}{\lambda r_p^{*2}}\cos\theta_p^*[2(\tilde{x}_u - \tilde{x}_p)m \\ &+ \frac{d}{r_p^*}(\tilde{x}_u - \tilde{x}_p)\sin\theta_p^* m^2 + \frac{d}{r_p^*}(\tilde{y}_u - \tilde{y}_p)\cos\theta_p^* m^2]\Gamma^{(m)}_{\theta_p^*, r_p^*}.\end{aligned} \tag{50}$$

APPENDIX B
PROOF OF THEOREM 1

We need to simplify the summations over m in (32), (33) and (34). To do this, we need the following summation:

$$\begin{aligned}\sum_{m=0}^{M-1} m^2 &= \frac{(M-1)M(M+1)}{6} \\ \sum_{m=0}^{M-1} m^3 &= \frac{(M-1)^2M^2}{4} \\ \sum_{m=0}^{M-1} m^4 &= \frac{(M-1)M(2M-1)(3M^2-3M-1)}{30}\end{aligned} \tag{51}$$

By considering trigonometric relation (7) and substituting the above summations into (32), (33) and (34), we get the following:

$$\begin{aligned}J_{\tilde{x}_u\tilde{x}_u} = \frac{2}{\sigma^2}\sum_{p=1}^{P}(\pi\frac{d}{\lambda r_p^{*2}}\cos\theta_p^*)^2[4\cos^2\theta_p^* r_p^{*2}\frac{(M-1)M(M+1)}{6} \\ + d^2\sin^2 2\theta_p^*\frac{(M-1)M(2M-1)(3M^2-3M-1)}{30} \\ + 4dr_p^*\cos\theta_p^*\sin 2\theta_p^*\frac{(M-1)^2M^2}{4}]\end{aligned} \tag{52}$$

$$J_{\tilde{x}_u\tilde{y}_u} = J_{\tilde{y}_u\tilde{x}_u} = -\frac{2}{\sigma^2}\sum_{p=1}^{P}(\pi\frac{d}{\lambda r_p^{*2}}\cos\theta_p^*)^2$$

$$[-2r_p^{*2}\sin 2\theta_p^*\frac{(M-1)M(M+1)}{6} + 2dr_p^*\cos 3\theta_p^*\frac{(M-1)^2M^2}{4} + d^2\frac{\sin 4\theta_p^*}{2}\frac{(M-1)M(2M-1)(3M^2-3M-1)}{30}] \tag{53}$$

$$J_{\tilde{y}_u\tilde{y}_u} = \frac{2}{\sigma^2}\sum_{p=1}^{P}(\pi\frac{d}{\lambda r_p^{*2}}\cos\theta_p^*)^2[4\sin^2\theta_p^* r_p^{*2}\frac{(M-1)M(M+1)}{6} + d^2\frac{\cos^2 2\theta_p^*}{2}\frac{(M-1)M(2M-1)(3M^2-3M-1)}{30} - 4dr_p^*\sin\theta_p^*\cos 2\theta_p^*\frac{(M-1)^2M^2}{4}] \tag{54}$$

Now, if $m \gg 1$, we can approximate (36) and (37) with their term that contains the highest power of M:

$$J_{11}^{-1} \approx \frac{3\sigma^2\lambda^2}{10\pi^2 M}\frac{\sum_{p=1}^{P}(\frac{\cos\theta_p^*}{r_p^*})^2\cos^2 2\theta_p^*}{g(\theta_1^*,\theta_2^*,\cdots\theta_P^*,r_1^*,\cdots,r_P^*)} \tag{55}$$

and

$$J_{22}^{-1} \approx \frac{3\sigma^2\lambda^2}{10\pi^2 M}\frac{\sum_{p=1}^{P}(\frac{\cos\theta_p^*}{r_p^*})^2\sin^2 2\theta_p^*}{g(\theta_1^*,\theta_2^*,\cdots\theta_P^*,r_1^*,\cdots,r_P^*)} \tag{56}$$

where $g(\theta_1^*,\theta_2^*,\cdots\theta_P^*,r_1^*,\cdots,r_P^*)$ is defined in (39). CRB is the trace of the matrix J^{-1} which is as follows:

$$CRB = J_{11}^{-1} + J_{22}^{-1} \approx \frac{3\sigma^2\lambda^2}{10\pi^2 M}\frac{\sum_{p=1}^{P}(\frac{\cos\theta_p^*}{r_p^*})^2}{g(\theta_1^*,\theta_2^*,\cdots\theta_P^*,r_1^*,\cdots,r_P^*)} \tag{57}$$

REFERENCES

[1] C. Feng, W. S. A. Au, S. Valaee, and Z. Tan, "Received-signal-strength-based indoor positioning using compressive sensing," *IEEE Trans. Mobile Comput.*, vol. 11, no. 2, pp. 1983–1993, Dec. 2012.

[2] W. Liu et al., "Survey on CSI-based indoor positioning systems and recent advances," in *Proc. Int. Conf. Indoor Positioning Indoor Navigat. (IPIN)*, Sep. 2019, pp. 1–8.

[3] J. Xiong and K. Jamieson, "ArrayTrack: A fine-grained indoor location system," in *Proc. USENIX Symp. Netw. Syst. Design Implement.*, 2013, pp. 71–84. [Online]. Available: https://www.usenix.org/conference/nsdi13/technical-sessions/presentation/xiong

[4] M. Kotaru, K. Joshi, D. Bharadia, and S. Katti, "SpotFi: Decimeter level localization using WiFi," in *Proc. ACM Conf. Special Interest Group Data Commun.*, Aug. 2015, pp. 269–282.

[5] M. T. Rahman, N. Tadayon, S. Han, and S. Valaee, "LocHunt: Angle of arrival based location estimation in harsh multipath environments," in *Proc. IEEE Global Commun. Conf. (GLOBECOM)*, Dec. 2018, pp. 1–6.

[6] M. T. Rahman, S. Han, N. Tadayon, and S. Valaee, "Ising model formulation of outlier rejection, with application in WiFi based positioning," in *Proc. IEEE Int. Conf. Acoust., Speech Signal Process. (ICASSP)*, May 2019, pp. 4405–4409.

[7] W. Gong and J. Liu, "RoArray: Towards more robust indoor localization using sparse recovery with commodity WiFi," *IEEE Trans. Mobile Comput.*, vol. 18, no. 6, pp. 1380–1392, Jun. 2019.

[8] S. Han, M. T. Rahman, and S. Valaee, "Angle of arrival and time of flight estimation as an Ising energy minimization problem," in *Proc. IEEE 31st Annu. Int. Symp. Pers., Indoor Mobile Radio Commun.*, Aug. 2020, pp. 1–6.

[9] S. Akbari and S. Valaee, "CAIM: Cooperative angle of arrival estimation using the Ising model," in *Proc. IEEE Globecom Workshops (GC Wkshps)*, Dec. 2021, pp. 1–6.

[10] J. Capon, "High-resolution frequency-wavenumber spectrum analysis," *Proc. IEEE*, vol. 57, no. 8, pp. 1408–1418, Aug. 1969.

[11] R. Schmidt, "Multiple emitter location and signal parameter estimation," *IEEE Trans. Antennas Propag.*, vol. AP-34, no. 3, pp. 276–280, Mar. 1986.

[12] R. Roy and T. Kailath, "Esprit-estimation of signal parameters via rotational invariance techniques," *IEEE Trans. Acoust., Speech, Signal Process.*, vol. 37, no. 7, pp. 984–995, Jul. 1989.

[13] H. Krim and M. Viberg, "Two decades of array signal processing research: The parametric approach," *IEEE Signal Process. Mag.*, vol. 13, no. 4, pp. 67–94, Jul. 1996.

[14] J. A. Fessler and A. O. Hero, "Space-alternating generalized expectation-maximization algorithm," *IEEE Trans. Signal Process.*, vol. 42, no. 10, pp. 2664–2677, Oct. 1994.

[15] A. Bazzi, D. T. M. Slock, L. Meilhac, and S. Panneerselvan, "A comparative study of sparse recovery and compressed sensing algorithms with application to AoA estimation," in *Proc. IEEE 17th Int. Workshop Signal Process. Adv. Wireless Commun. (SPAWC)*, Jul. 2016, pp. 1–5.

[16] E. J. Candes and M. B. Wakin, "An introduction to compressive sampling," *IEEE Signal Process. Mag.*, vol. 25, no. 2, pp. 21–30, Mar. 2008.

[17] Q. H. Spencer, B. D. Jeffs, M. A. Jensen, and A. L. Swindlehurst, "Modeling the statistical time and angle of arrival characteristics of an indoor multipath channel," *IEEE J. Sel. Areas Commun.*, vol. 18, no. 3, pp. 347–360, Mar. 2000.

[18] S. Azzouzi, M. Cremer, U. Dettmar, R. Kronberger, and T. Knie, "New measurement results for the localization of UHF RFID transponders using an angle of arrival (AoA) approach," in *Proc. IEEE Int. Conf. RFID*, Apr. 2011, pp. 91–97.

[19] A. J. Weiss, "Direct position determination of narrowband radio frequency transmitters," *IEEE Signal Process. Lett.*, vol. 11, no. 5, pp. 513–516, May 2004.

[20] M. Wax and T. Kailath, "Optimum localization of multiple sources by passive arrays," *IEEE Trans. Acoust., Speech, Signal Process.*, vol. ASSP-31, no. 5, pp. 1210–1217, Oct. 1983.

[21] K. Papakonstantinou and D. Slock, "Direct location estimation using single-bounce NLOS time-varying channel models," in *Proc. IEEE 68th Veh. Technol. Conf.*, Sep. 2008, pp. 1–5.

[22] O. Bialer, D. Raphaeli, and A. J. Weiss, "Maximum-likelihood direct position estimation in dense multipath," *IEEE Trans. Veh. Technol.*, vol. 62, no. 5, pp. 2069–2079, Jun. 2013.

[23] N. Garcia, H. Wymeersch, E. G. Larsson, A. M. Haimovich, and M. Coulon, "Direct localization for massive MIMO," *IEEE Trans. Signal Process.*, vol. 65, no. 10, pp. 2475–2487, May 2017.

[24] E. T. Northardt, I. Bilik, and Y. I. Abramovich, "Spatial compressive sensing for direction-of-arrival estimation with bias mitigation via expected likelihood," *IEEE Trans. Signal Process.*, vol. 61, no. 5, pp. 1183–1195, Mar. 2013.

[25] F. Zafari, A. Gkelias, and K. K. Leung, "A survey of indoor localization systems and technologies," *IEEE Commun. Surveys Tuts.*, vol. 21, no. 3, pp. 2568–2599, 3rd Quart., 2019.

[26] J. Xiao, Z. Zhou, Y. Yi, and L. M. Ni, "A survey on wireless indoor localization from the device perspective," *ACM Comput. Surv.*, vol. 49, no. 2, pp. 1–31, Jun. 2016.

[27] H. Liu, H. Darabi, P. Banerjee, and J. Liu, "Survey of wireless indoor positioning techniques and systems," *IEEE Trans. Syst. Man, Cybern. C, Appl. Rev.*, vol. 37, no. 6, pp. 1067–1080, Nov. 2007.

[28] S. Kumar, S. Gil, D. Katabi, and D. Rus, "Accurate indoor localization with zero start-up cost," in *Proc. 20th Annu. Int. Conf. Mobile Comput. Netw.*, Sep. 2014, pp. 483–494.

[29] W. Dargie, *Fundamentals of Wireless Sensor Networks: Theory and Practice*. Hoboken, NJ, USA: Wiley, 2010.

[30] B. G. Lee and S. Choi, *Broadband Wireless Access and Local Networks: Mobile WiMAX and WiFi*. Norwood, MA, USA: Artech House, 2008.

[31] M. Kohne and J. Sieck, "Location-based services with iBeacon technology," in *Proc. 2nd Int. Conf. Artif. Intell., Modeling Simulation*, Nov. 2014, pp. 315–321.

[32] P. Baronti, P. Pillai, V. W. C. Chook, S. Chessa, A. Gotta, and Y. F. Hu, "Wireless sensor networks: A survey on the state of the art and the 802.15.4 and ZigBee standards," *Comput. Commun.*, vol. 30, no. 7, pp. 1655–1695, May 2007.

[33] B. Hanssens et al., "An indoor localization technique based on ultra-wideband AoD/AoA/ToA estimation," in *Proc. IEEE Int. Symp. Antennas Propag. (APSURSI)*, Jun. 2016, pp. 1445–1446.

[34] X. Bai, Z. Zhang, L. Liu, X. Zhai, J. Panneerselvam, and L. Ge, "Enhancing localization of mobile robots in distributed sensor environments for reliable proximity service applications," *IEEE Access*, vol. 7, pp. 28826–28834, 2019.

[35] W. Cui, C. Wu, W. Meng, B. Li, Y. Zhang, and L. Xie, "Dynamic multidimensional scaling algorithm for 3-D mobile localization," *IEEE Trans. Instrum. Meas.*, vol. 65, no. 12, pp. 2853–2865, 2016.

[36] A. Amar and A. J. Weiss, "Direct position determination of multiple radio signals," in *Proc. IEEE Int. Conf. Acoust., Speech, Signal Process.*, Sep. 2004, p. 81.

[37] Z. Shen, K. Xu, and X. Xia, "2D fingerprinting-based localization for mmWave cell-free massive MIMO systems," *IEEE Commun. Lett.*, vol. 25, no. 11, pp. 3556–3560, Nov. 2021.

[38] B. Wang, X. Liu, B. Yu, R. Jia, and X. Gan, "An improved WiFi positioning method based on fingerprint clustering and signal weighted Euclidean distance," *Sensors*, vol. 19, no. 10, p. 2300, May 2019.

[39] D. Sikeridis, B. P. Rimal, I. Papapanagiotou, and M. Devetsikiotis, "Unsupervised crowd-assisted learning enabling location-aware facilities," *IEEE Internet Things J.*, vol. 5, no. 6, pp. 4699–4713, Dec. 2018.

[40] J. Choi, Y.-S. Choi, and S. Talwar, "Unsupervised learning technique to obtain the coordinates of Wi-Fi access points," in *Proc. Int. Conf. Indoor Positioning Indoor Navigat. (IPIN)*, Sep. 2019, pp. 1–6.

[41] F. Dou, J. Lu, Z. Wang, X. Xiao, J. Bi, and C.-H. Huang, "Top-down indoor Localization with Wi-Fi fingerprints using deep Q-network," in *Proc. IEEE 15th Int. Conf. Mobile Ad Hoc Sens. Syst. (MASS)*, Jun. 2018, pp. 166–174.

[42] H. Zou, Y. Zhou, H. Jiang, B. Huang, L. Xie, and C. Spanos, "Adaptive localization in dynamic indoor environments by transfer kernel learning," in *Proc. IEEE Wireless Commun. Netw. Conf. (WCNC)*, Mar. 2017, pp. 1–6.

[43] F. Yin et al., "FedLoc: Federated learning framework for data-driven cooperative localization and location data processing," *IEEE Open J. Signal Process.*, vol. 1, pp. 187–215, 2020.

[44] L. Zhao, H. Huang, X. Li, S. Ding, H. Zhao, and Z. Han, "An accurate and robust approach of device-free localization with convolutional autoencoder," *IEEE Internet Things J.*, vol. 6, no. 3, pp. 5825–5840, Jun. 2019.

[45] S. E. Trevlakis et al., "Localization as a key enabler of 6G wireless systems: A comprehensive survey and an outlook," *IEEE Open J. Intell. Comun. Soc.*, vol. 4, pp. 2733–2801, Jan. 2023.

[46] M. T. Rahman and S. Valaee, "Location estimates from channel state information via binary programming," *IEEE Trans. Signal Process.*, vol. 70, pp. 5265–5278, 2022.

[47] S. Akbari and S. Valaee, "Direct localization: An Ising model approach," in *Proc. IEEE Int. Conf. Acoust., Speech Signal Process. (ICASSP)*, May 2022, pp. 5138–5142.

[48] D. J. MacKay, *Information Theory, Inference and Learning Algorithms*. Cambridge, U.K.: Cambridge Univ. Press, 2003.

[49] A. Harju, T. Siro, F. F. Canova, S. Hakala, and T. Rantalaiho, "Computational physics on graphics processing units," in *Proc. Int. Workshop Appl. Parallel Comput.* Cham, Switzerland: Springer, 2012, pp. 3–26.

[50] M. Lewis and F. Glover, "Quadratic unconstrained binary optimization problem preprocessing: Theory and empirical analysis," *Networks*, vol. 70, no. 2, pp. 79–97, Sep. 2017.

[51] A. Lucas, "Ising formulations of many NP problems," *Frontiers Phys.*, vol. 2, p. 5, Jan. 2014.

[52] S. Boixo et al., "Evidence for quantum annealing with more than one hundred qubits," *Nature Phys.*, vol. 10, pp. 218–224, Feb. 2014.

[53] S. Matsubara et al., "Digital annealer for high-speed solving of combinatorial optimization problems and its applications," in *Proc. 25th Asia South Pacific Design Autom. Conf. (ASP-DAC)*, Jan. 2020, pp. 667–672.

[54] M. Aramon, G. Rosenberg, E. Valiante, T. Miyazawa, H. Tamura, and H. G. Katzgraber, "Physics-inspired optimization for quadratic unconstrained problems using a digital annealer," *Frontiers Phys.*, vol. 7, p. 48, Apr. 2019.

[55] A. N. Bishop, B. D. O. Anderson, B. Fidan, P. N. Pathirana, and G. Mao, "Bearing-only localization using geometrically constrained optimization," *IEEE Trans. Aerosp. Electron. Syst.*, vol. 45, no. 1, pp. 308–320, Jan. 2009.

[56] F. Gringoli, M. Schulz, J. Link, and M. Hollick, "Free your CSI: A channel state information extraction platform for modern Wi-Fi chipsets," in *Proc. 13th Int. Workshop Wireless Netw. Testbeds, Exp. Eval. Characterization*, Oct. 2019, pp. 21–28.

[57] N. Tadayon, M. T. Rahman, S. Han, S. Valaee, and W. Yu, "Decimeter ranging with channel state information," *IEEE Trans. Wireless Commun.*, vol. 18, no. 7, pp. 3453–3468, Jul. 2019.

[58] Y. D. J. Bultitude and T. Rautiainen, "IST-4-027756 WINNER II D1. 1.2 V1. 2 WINNER II channel models," EBITG, TUI, UOULU, CU/CRC, NOKIA, Tech. Rep., 2007.

Shiva Akbari (Graduate Student Member, IEEE) received the B.Sc. and M.Sc. degrees in electrical and computer engineering from the University of Tehran, Tehran, Iran. She is currently pursuing the Ph.D. degree with The Edward S. Rogers Sr. Department of Electrical and Computer Engineering, University of Toronto. Her research focuses on signal processing and optimization in wireless communications, particularly for location estimation applications. Her research interests include signal processing, machine learning, and optimization. She was a recipient of the Edward S. Rogers Sr. Department Award, highlighting her contributions and excellence in her field.

Shahrokh Valaee (Fellow, IEEE) is currently a Professor with The Edward S. Rogers Sr. Department of Electrical and Computer Engineering, University of Toronto, and the holder of the Nortel Chair of Network Architectures and Services. He is also the Founder and the Director of the Wireless Innovation Research Laboratory (WIRLab), University of Toronto. He is a fellow of the Engineering Institute of Canada. He was a co-recipient of the Best Paper Award at the IEEE Machine Learning for Signal Processing (MLSP) 2020 Workshop. He was the TPC Co-Chair and the Local Organization Chair of the IEEE Personal Mobile Indoor Radio Communication (PIMRC) Symposium 2011; the TPC Co-Chair of ICT 2015 and PIMRC 2017; the Track Co-Chair of WCNC 2014, PIMRC 2020, and VTC Fall 2020; and the Co-Chair of the Organizing Committee for PIMRC 2023. From December 2010 to December 2012, he was an Associate Editor of IEEE SIGNAL PROCESSING LETTERS. From 2010 to 2015, he was an Editor of IEEE TRANSACTIONS ON WIRELESS COMMUNICATIONS. He is currently an Editor of *Journal of Computer and System Science*. From 2021 to 2023, he was a Distinguished Lecturer of the IEEE Communications Society. He serves as a Distinguished Lecturer for the IEEE Vehicular Technology Society.